Surface & Coatings Technology 490 (2024) 131187

Contents lists available at ScienceDirect

Surface & Coatings Technology

journal homepage: www.elsevier.com/locate/surfcoat

Controllable stress-adsorbed layers in Ti/TiN/TiAlN coatings: Mechanical performance and micropillar compression

Jingjun Yan [a,b], Zhenyu Wang [a,*], Shenghao Zhou [a], Guanshui Ma [a], Dingwei Zhou [a], Wei Yang [a], Aiying Wang [a,b,*]

[a] Key Laboratory of Advanced Marine Materials, Ningbo Institute of Materials Technology and Engineering, Chinese Academy of Sciences, Ningbo 315201, China
[b] Center of Materials Science and Optoelectronics Engineering, University of Chinese Academy of Sciences, Beijing 100049, China

ARTICLE INFO

Keywords:
Multilayer coatings
Mechanical properties
Erosion resistance
Uniaxial compression
Stress-absorbed layers

ABSTRACT

Solid particle erosion often compromises the durability of turbine engine blades, particularly those used in offshore and desert environments. Surface protective coatings have emerged as a promising solution to significantly enhance the erosion resistance of compressor blades. In this study, TiAlN multilayer coatings were deposited onto Ti-6Al-4V substrates using a vacuum arc deposition technique. The article explored the strategic incorporation of TiN-Ti-TiN stress-adsorbed layers (SALs) within TiAlN-based coatings. It also investigated the microscale mechanisms leading to coating failure under conditions of micropillar compression. The findings revealed that the presence of metal/ceramic interfaces significantly improved the adhesion strength, crack resistance, erosion resistance and fracture toughness of the coatings. The multilayer deformation behavior of the coatings was primarily determined by the plastic flow of the softer metal layers. The SALs played a crucial role in reducing the elastic strain energy by generating nanotwins, coherent interfaces, and high-density dislocations during deformation, thereby improving the coatings' plastic deformation capability. Moreover, the implementation of dual-cycle SALs successfully reduced radial crack propagation, facilitating a transition from brittle fracture to a combined brittle-ductile fracture mechanism. This study highlights the critical role of metal/ceramic interfaces and SALs in improving the erosion resistance and co-deformability of TiAlN-based hard coatings.

1. Introduction

Titanium alloys are frequently employed in the manufacture of compressor components for aero-engines and gas turbines due to their exceptional specific strength, low density, and superior mechanical attributes. During low-altitude flights, takeoffs and landings, atmospheric particles of salt, volcanic ash, snow and sand present are inevitably drawn into the engines. These particles can cause significant erosion, wear, and even deformation of the blades [1]. Additionally, in offshore operations, carrier-based aircraft blades are prone to salt corrosion, adversely affecting engine performance and increasing maintenance costs. The use of binary nitride coatings like TiN and ZrN, along with low-temperature aluminized-silicate composite coatings, has proven effective in protecting compressor blades [2]. However, these erosion-resistant coatings are relatively brittle, which increases the likelihood of surface crack initiation, thereby diminishing the fatigue resistance of the alloy. Addressing this technical challenge is imperative. Metal/ceramic multilayer coatings have emerged as a leading protective technology to combat this issue. These coatings combine high toughness with hardness, resulting in enhanced erosion resistance [3]. The multilayer structure of the coatings allows for the ductile layers to absorb strain energy through plastic deformation, while the ceramic layers provide impact and wear resistance [4]. The integration of Al into binary ceramic coatings, such as TiN, leads to the formation of multi-component alloys that significantly enhance the erosion-corrosion resistance of the coatings [5]. This improvement in fracture toughness facilitates the development of multi-layer composite structures like Ti-TiN-TiAlN, which demonstrate superior erosion resistance under complex operational conditions. Several studies have confirmed the effectiveness of this structure in managing residual stress, reducing stress concentration, and limiting the propagation of penetrating cracks [6,7]. Despite considerable advancements, current research predominantly focuses on macroscopic performance of coatings, with little attention given to the role of multilayer interfaces in enhancing micro-nano

* Corresponding authors.
E-mail addresses: wangzy@nimte.ac.cn (Z. Wang), aywang@nimte.ac.cn (A. Wang).

https://doi.org/10.1016/j.surfcoat.2024.131187
Received 11 June 2024; Received in revised form 8 July 2024; Accepted 27 July 2024
Available online 29 July 2024

mechanical properties. Exploring the micromechanical behavior at heterogeneous interfaces is crucial for a deeper understanding of the toughening mechanisms in multilayer coatings [8].

Uniaxial compression testing has played a crucial role in examining the micro-scale deformation behavior of materials during yielding. The deformation constraint, which arises from the disparate elastic-plastic properties in composite coatings, plays a pivotal role in the mechanical behavior of these materials [9,10]. Lotfian et al. [11] showed that in Al/SiC multilayer coatings, the stiff and elastic SiC layers constrained the plastic deformation of the soft layers at room temperature. This phenomenon was responsible for the large strain hardening rate and high hardness observed in these coatings. At high temperatures, limited extrusions of Al layers were observed from the micropillar and there was a notable decrease in the hardening rate. Yang et al. [12] linked the mechanical response of Al/SiC nanolaminates made of materials with a large difference in the elasto-plastic properties to the critical role played by constraint. They demonstrated that when the thickness of the soft layers is relatively large, the effect of the elastic constraint of ceramic layers is limited, with deformation primarily accommodated by the plastic flow of the Al. Doan et al. [13] investigated the deformation behavior and mechanical characteristic of TiN/Al bilayer composites under the nanoindentation. The results exposed that the interface as a barrier against the spread of stress and strain into the substrate interior. The research also discussed the thorough effect of the layer size in improved plastic co-deformation capacity in TiN/Al composites. Similar results have also been documented by Yang et al. [14] in their investigation of interface characteristics and plastic deformation mechanisms under compressive loading in Ti/TiN multilayers with a semi-coherent interface using MD simulations. Studies of Cu-TiN multilayer nanocomposites according to Wheeler et al. [15] showed that the deformation of Cu in the nanolaminates dominated the plastic response in these composites and a decrease in the apparent activation energy value indicated possible co-deformation of Cu and TiN. Metal/ceramic multilayer coatings often exhibit a strengthening effect. However, the relationship between mechanical properties and the sublayer scale varies across systems [10]. Therefore, a more comprehensive characterization and theoretical explanation of the mechanical behavior at the metal/nitride interfaces during deformation and the elastic-plastic deformation mechanisms in multilayer structures is necessary.

TiAlN-based coatings are commonly used for erosion protection due to their outstanding hardness and wear resistance [16]. Ti/TiN/TiAlN multilayer structure has been developed to further enhance the overall mechanical properties [17]. Previous research has shown that Ti/TiN/TiAlN multilayer coatings have the best bond strength, oxidation resistance, and erosion resistance when the thickness ratio of the Ti bottom layer to the TiN carrier layer is 1:2 [18,19]. The erosion resistance of the Ti/TiAlN coatings was improved by the presence of a Ti layer and the multilayer interfaces. This hindered radial crack propagation and confined transverse cracks within a single TiAlN layer [5,20]. However, there is limited data on the toughening mechanisms of the metal layers in enhancing the mechanical properties of multilayer coatings.

This paper presents a description of deposition of Ti/TiN/TiAlN multilayer coatings on titanium alloy substrates using a proprietary cathode vacuum multi-arc ion plating system. The coatings were deposited with varying amounts of SALs. The study evaluated the erosion resistance and micro-nano mechanical behavior of the coatings. Furthermore, the research investigated the anti-crack extension and toughening mechanisms of the ductile layers during the deformation process. This study offers new theoretical insights into the application of protective coatings on compressor blades and provides a framework for the design of multifunctional coatings.

2. Experimental

2.1. Coating deposition

Ti/TiN/TiAlN multilayer coatings were deposited onto Ti-6Al-4V (TC4) substrates by cathode vacuum arc ion plating. Samples produced by vacuum arc deposition exhibit higher deposition efficiency, strong bond strength, and excellent mechanical properties [21]. These benefits arise from the high degree of ionization, ion energy, and plasma generation rate in the cathode spot [22]. A schematic diagram of the deposition system is presented in Fig. 1. The system consists of four independent cathodic arc sources and one linear ion beam (LIS) source. The LIS source is used to etch the sample surfaces and remove impurities thoroughly. Four arc targets are strategically positioned on either side of the deposition chamber, each with a diameter of 128 mm. Ti targets with a purity of 99.9 wt% were employed for the deposition of the Ti layer and TiN layer. The TiAlN layer was deposited using TiAl targets with a Ti:Al atomic ratio of 33:67. Prior to deposition, all substrates underwent mechanical polishing with SiC sandpaper up to 5000 grit, followed by ultrasonic cleaning in acetone and ethanol for 10 min each. During the coating preparation phase, the deposition temperature for the samples was consistently maintained at 300 ± 5 °C. A Ti buffer layer was first deposited under an Ar atmosphere to enhance adhesion strength. Argon was used as the protective gas during the Ti layer deposition, with a flow rate of 200 sccm and a deposition pressure of 45 mTorr. For the deposition of TiN and TiAlN layers, N_2 was used as the reactive gas, with flow rates of 500 sccm and deposition pressures of 45 mTorr and 55 mTorr, respectively. The deposition process utilized self-rotating jigs that advanced in front of different ion sources via the chassis. For detailed parameters, please refer to Table 1.

Controllable SALs were incorporated into the Ti/TiN/TiAlN multilayer coatings. The TiN-Ti-TiN gradient structures were used to create the SALs. The Ar/N_2 flux ratio was adjusted alternately during the Ti and TiN layer depositions, as detailed in Table 2. Figs. S1 and S2 show the structural characterization and mechanical properties of the samples with different numbers of SALs. When the coating thickness remains constant, the continuous addition of the SALs leads to a significant deterioration in the service performance of the coatings. The dual-cycle SALs sample exhibits excellent deformation co-ordination and comprehensive mechanical properties. This study mainly explores the strengthening mechanism of monolithic TiAlN coatings and TiAlN-based coatings with dual-cycle SALs, labeled as TiAlN-0SAL and TiAlN-2SAL, respectively.

2.2. Characterization methods

The surface and cross-sectional morphologies of the deposited materials and scratch tracks were examined using a field-emission scanning electron microscope (FEI Quanta FEG 250). The chemical composition of the coatings was analyzed using energy dispersive X-ray spectroscopy (EDS) at an accelerating voltage of 20 kV. Scratch tests (CSM Revetest, Switzerland) were conducted on the coating surfaces to evaluate their adhesion strength and resistance to crack propagation. An indenter traversed 5 mm across the coating at a speed of 2 mm/min, with the load incrementally increasing from 1 N to 100 N. To ensure the reliability of the results, each sample underwent a minimum of three tests. The hardness and Young's modulus of the deposited coatings were measured using a nanoindenter (G200, MTS) equipped with a Berkovich indenter via continuous stiffness measurement (CSM). To eliminate the influence of metallic macro-particles, all samples were polished using a ball cratering apparatus before testing. The Oliver and Pharr model was applied to determine the hardness and elastic modulus values.

The surface fracture toughness of the coating was assessed using a cube-corner diamond indenter with a face angle of 65.3°. This was achieved by analyzing the small-scale cracks that formed around the indentations [23,24]. Post-nanoindentation surface morphology was

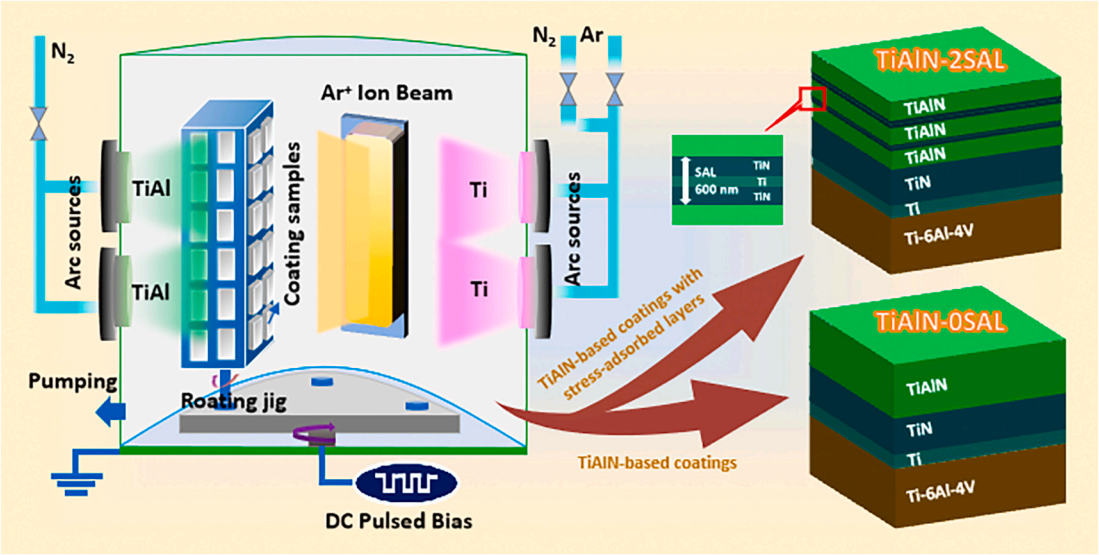

Fig. 1. Schematic illustrations of deposition system and coating structure: Ti/TiN/TiAlN multilayer coatings with controllable TiN-Ti-TiN stress-adsorbed layers.

Table 1
Process parameters of cleaning and deposition.

Procedure	Flow (sccm)		Current (A)			Chamber pressure (mTorr)	Substrate bias (V)	Time (min)
	Ar	N_2	Linear ion beam	Ti cathodes	TiAl cathodes			
Ion etching	35	0	0.2	–	–	1.5	−200	30
Buffer layer	200	0	–	70	–	45.0	−70	28
Transition layer	0	500	–	70	–	45.0	−70	80
Top layer	0	500	–	–	80	55.0	−80	100/45/27

Table 2
Deposition process for a single SAL.

Sublayer structure	N_2 flow (sccm)	Ar flow (sccm)	Time (min)
TiN layer	From 200 to 0	From 0 to 200	3
Ti layer	0	200	6
TiN layer	0 back to 200	200 back to 0	3

captured using the conductive atomic force microscope (C-AFM) mode in a scanning probe microscope (SPM, Bruker). The microstructural evolution of the coatings was characterized through transmission electron microscopy (TEM, Talos F200×).

2.3. Erosion test

The erosion test platform has been developed in accordance with the solid particle erosion test standards of the American Society for Testing and Materials (ASTM G76-18, ASTM G76-13). Compressed air is used to accelerate erosion particles towards the coating surface at high velocities. The gas pressure is adjustable, allowing for precise control over the particles' speed and energy. Further details on the apparatus can be found in our prior research [18]. The test parameters involve using polygonal quartz sand with a particle size of approximately 180 μm as the erosion medium. The erosion angle is fixed at 90°, and the total mass of the particles is set to 10.0 ± 0.5 g. The powder feeding rate remains at 2 ± 0.2 g/min. The weight loss method is used to determine the erosion rate, which indicates the coating's erosion resistance. The change in mass of the samples during the erosion test was measured using an analytical balance (Mettler Toledo, XS205 DU) with a resolution of 0.01 mg. Prior to and following testing, the samples were cleaned with absolute ethanol for 10 min and subsequently dried. To ensure the reliability of the results, a minimum of three tests were performed on each sample.

2.4. Micropillar compression test

Micropillars with a diameter of 1.2 μm and a height of 3.6 μm were produced using a dual-beam focused ion beam (Helios-G4-CX) with an accelerating voltage of 30 keV. The aspect ratio of the micropillars was kept below 3:1 to prevent bending or flexing during compression, ensuring uniform compression without end effects [25]. It should be noted that micropillars of this height can contain multiple SALs. All micropillars underwent the same annulus milling process. To prepare the coarse pillars initially, a beam current of 9.3 nA was used for those with a diameter greater than 1.5 μm and a height less than 3 μm. Subsequently, these pillars were further refined using a beam current of 1 nA and finally polished with a beam current of 80 pA to minimize surface damage and roughness. The final milling step, using a low current, was crucial for minimizing taper and reducing potential damage from the Ga^+ ion source to the micropillar surface [26].

The Bruker TI 980 Triboindenter with a flat-punch diamond indenter was used to conduct uniaxial compression testing. Each type was tested with at least three micropillars, and all loading functions were displacement controlled. Engineering stress and strain were calculated using the formulas $\sigma = F/A0$ and $\varepsilon = \Delta h/h0$, where F represents the compressive load, A0 the initial cross-sectional area, Δh the punch displacement, and h0 the original height of the micropillars respectively [27]. To explain the deformation mechanism, we deposited protective layers of Pt and C on the micropillars using a Ga^+ ion beam in FIB. After encasing the samples with protective layers, we thinned them to electron transparency for TEM analysis.

3. Results and discussion

3.1. Microstructure characterization

Fig. 2(a–d) displays the cross-sectional morphologies of the as-deposited coatings, which maintained a total thickness of approximately 10.5 μm. The coating structure consisted of a 1.5 μm thick Ti bottom layer, a 3 μm thick TiN load-bearing layer, and a controllably inserted 0.5 μm thick SAL. The Ti layer acted as a transition between the substrate and the coating, enhancing adhesion, while the TiN layer provided load-bearing capacity and established a hardness gradient between the Ti and TiAlN layers. The erosion resistance of the material was attributed to the superior mechanical properties of the TiAlN layer [18]. The EDS results showed distinct interfaces between the sublayers in the multilayer structure, as well as significant compositional contrasts. Fig. 2(e) displays the STEM images of the as-deposited SAL, with EDS mapping (Fig. 2(f)) indicating clear interfaces and uniform compositions. Line scan results (Fig. 2(g)) along the growth direction of SAL revealed a sandwich-like gradient structure. The HRTEM and SAED results (Fig. 2(h)) confirmed that the Ti, TiN, and TiAlN sublayers maintained a stable phase structure without undergoing any phase transitions.

3.2. Mechanical properties

3.2.1. Adhesion strength

The study evaluated the adhesion strength of multilayer coatings using a progressive micron scratch test. Scratch morphologies for coatings are shown in Fig. 3(a–b). The critical load at which the substrates were exposed during the scratch test was used to determine the adhesion strength [18,28]. The results indicated that the adhesion strength of the coatings improved with the addition of dual-SALs. TiAlN-0SAL samples were susceptible to cracking, displaying river-like crack patterns when subjected to scratching [29]. The TiAlN-2SAL coatings, on the other hand, did not exhibit the 'river pattern' brittle peeling at the scratch edge, indicating stronger crack resistance. The buckle spallation failure mode was observed at the critical load of Lc3, defined as the load corresponding to the substrate exposure [28]. The EDS mappings in Fig. 3 (c–d) showed significant vanadium enrichment, confirming the complete exposure of the TC4 substrates. The incorporation of SALs mitigated the cohesive damage in the monolithic TiAlN coatings, thereby increasing the adhesion strength of the multilayer coatings from 52.1 N to 67.9 N.

SEM images taken at the load of 30 N (Fig. 3(e–f)) show significant plastic deformation without exposing the substrate. The TiAlN-0SAL samples exhibited continuous corrugated tensile cracks within the scratch and numerous microcracks at the scratch edge. This was a typical result of hard coating scratching on soft substrates due to tensile stress and friction [30]. At a 30 N load, the indenter tip penetrated the top layer of TiAlN-2SAL samples, revealing a metallic luster indicative of the soft metal beneath. The presence of short and sparse cracks at the scratch edges decreased with the introduction of dual-cycle SALs. Cross-sectional morphologies beneath the indenter of 30 N (Fig. 3(g–h)) show that TiAlN-0SAL samples developed multiple radial cracks extending in the coating growth direction. Under bending stresses, the surface and substrate areas experienced compressive and tensile stresses, respectively, resulting in the formation of radial cracks [31]. The addition of SALs resulted in crack deflection and disappearance, with the alternating soft/hard interface structure of the SALs playing a crucial role in coordinating deformation and absorbing stress [32]. The TiAlN-2SAL samples effectively reduced the generation and extension of radial cracks during deformation by inducing plastic deformation through multiple SALs. Additionally, they prevented delamination fracture that was initiated by the accumulation of transverse cracks at the interfaces.

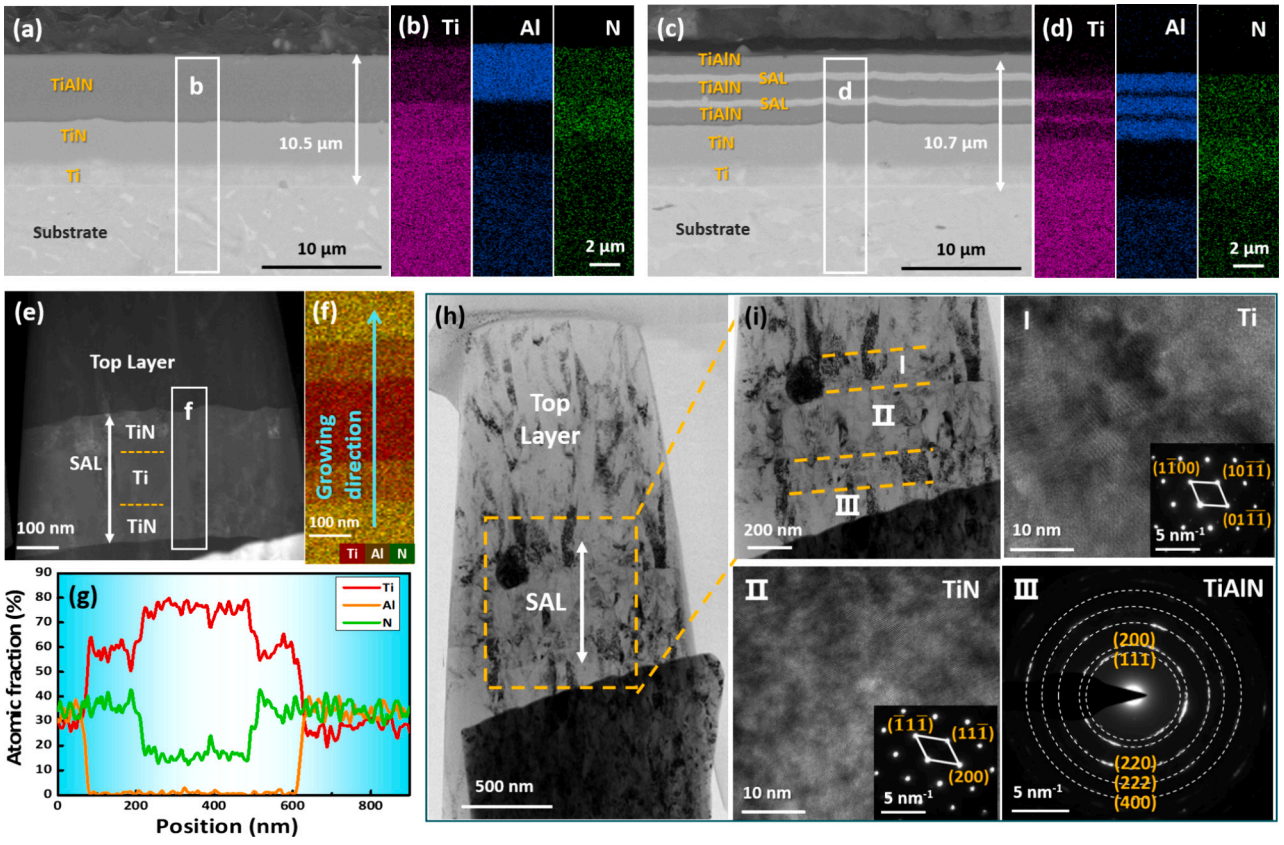

Fig. 2. SEM images and cross-sectional EDS mappings of (a–b) TiAlN-0SAL, (c–d) TiAlN-2SAL samples; (e) STEM images and (f–g) EDS line scanning of the as-deposited SAL along the growing direction, (h–i) component characteristics of each sublayer.

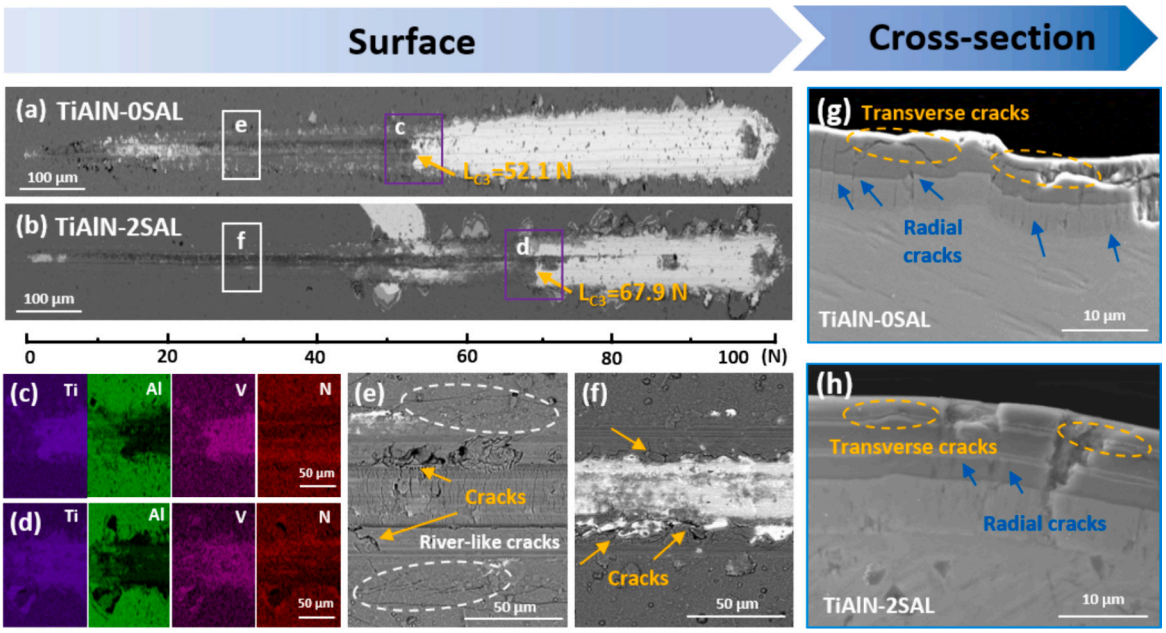

Fig. 3. Adhesion strength and crack resistance of different simples: surface morphologies of (a) TiAlN-0SAL and (b) TiAlN-2SAL after scratching, (c–d) corresponding EDS mapping results in the initial peeling area, (e–f) surface and (g–h) cross-sectional scratch morphologies under the load of 30 N.

3.2.2. *Surface fracture toughness*

The use of sharp cube corner indenters can significantly reduce the indentation-cracking threshold, allowing for the measurement of fracture toughness with minimal loading force [33]. In preliminary experiments, radial cracks were observed at the indentation tips of coatings under a maximum load of 300 mN. The surface morphologies after nanoindentation, depicted in Fig. 4(a–b), revealed radial cracks at the indentation tips and varying degrees of plastic deformation across the coating surfaces. This deformation aids in stress relaxation within the material and absorbs substantial strain energy, thus limiting radial crack propagation. This behavior serves as a basis for estimating the fracture toughness of the coatings [34]. The TiAlN-0SAL samples exhibited longer crack lengths at the indentation tips compared to the TiAlN-2SAL samples, with both showing significant plastic accumulation at the

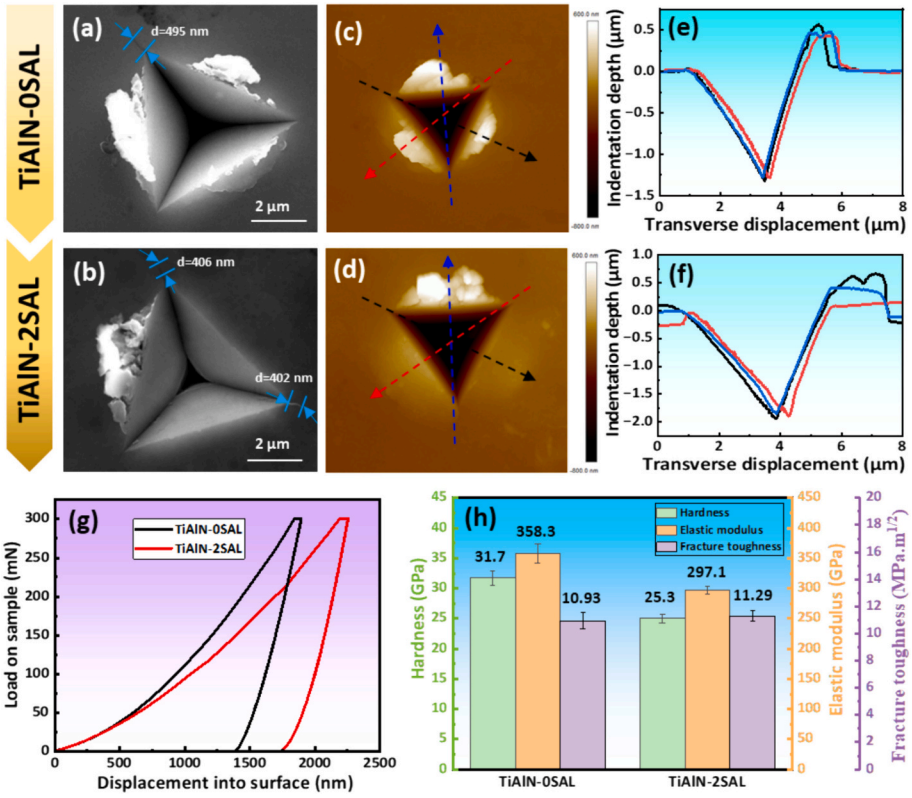

Fig. 4. Surface fracture toughness measured using a cube-corner indenter: (a–b) indentation morphologies at 300 mN, (c–d) AFM surface morphologies, (e–f) apparent height variations of the indentations, (g) load-displacement curves and (h) micromechanical properties of Ti/TiN/TiAlN coatings.

indentation edges. The AFM height images (Fig. 4(c–d)) provided morphological details that were consistent with the SEM observations. Fig. 4(e–f) shows the apparent height variations of the indentations captured by AFM, revealing that the maximum indentation depth and width increased with SALs under the same load. The mechanical property alterations in the coatings are responsible for this. The TiAlN-0SAL samples, which have the highest hardness and thickest sublayer, exhibited the smallest indentation under identical conditions. The introduction of SALs helps to alleviate the high stress distribution by facilitates plastic deformation, resulting in broader and deeper indentations. These findings are supported by the load-depth curves in Fig. 4(g), particularly with regard to spring-back depth.

The measurement results of surface fracture toughness are shown in Fig. 4(h) [22]. The TiAlN-2SAL samples exhibited the highest fracture toughness (11.29 MPa·$m^{1/2}$), outperforming the TiAlN-0SAL samples. The superior toughness of the TiAlN-2SAL samples is attributed to the effective stress relaxation of the SALs and the optimal matching of the multilayer structure. The hardness and Young's modulus of the multilayer coatings were evaluated using the continuous stiffness method with a Berkovich indenter. To mitigate the influence of the substrate on the coatings' hardness, the indentation depth was limited to no more than one-tenth of the total coating thickness [35]. Fig. 4(h) also illustrates the hardness values for the TiAlN-0SAL and TiAlN-2SAL samples, recorded at 31.7 ± 1.37 GPa and 25.3 ± 0.83 GPa, respectively. The corresponding Young's modulus were 358.3 ± 15.8 GPa and 297.1 ± 6.2 GPa. A trend was observed where both the Young's modulus and hardness decreased with an increase in SALs (Fig. S2). This reduction is attributed to the incorporation of relatively softer sublayers within the TiAlN hard layer [20]. The metal layer's uniform distribution is further enhanced by the addition of SALs [36]. TiAlN-2SAL samples result in an enhancement of the comprehensive mechanical properties through an optimized multilayer structure design.

3.2.3. Erosion resistance

Fig. 5 illustrates the erosion rates of various samples using polygonal quartz sand. The erosion rate of the substrates was four times higher than that of the TiAlN-0SAL samples. The addition of SALs within the TiAlN functional layer significantly enhanced erosion resistance, with the TiAlN-2SAL samples demonstrating the best performance (0.04 ± 0.008 mg/g). The modulation period of the ductile layers in the multilayer structure is crucial to the coatings' mechanical response [24]. Differences in adhesion strength between sublayers can lead to delamination at the interfaces, reducing the load-bearing capacity. Moreover, high residual stress within the coatings can exacerbate the propagation of penetration-type cracks and delamination fractures. By optimizing the number of SAL cycles and the thickness ratio, the dual-SAL structure effectively leverages the hard layer's impact and wear resistance alongside the soft layer's high toughness, significantly enhancing erosion resistance.

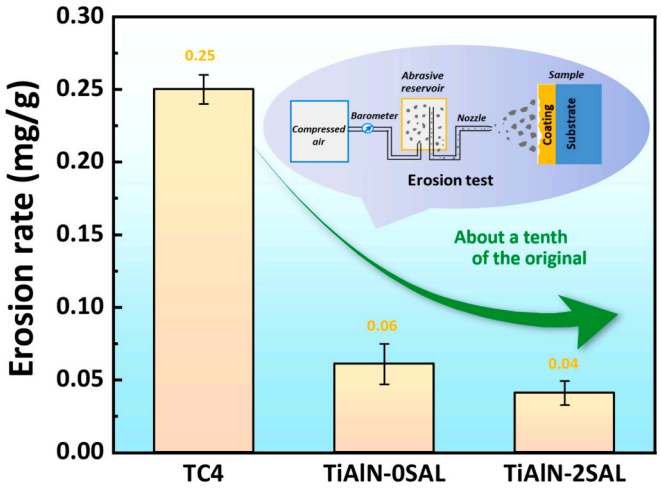

Fig. 5. Erosion result of Ti/TiN/TiAlN coatings with different amounts of SALs.

3.3. Deformation behavior of micropillars after compression

3.3.1. Compressed morphologies and stress-strain curves

The micro-scale deformation behavior of the coatings was explored through micropillar compression test. Fig. S3 shows the micropillar structures of TiAlN-0SALand TiAlN-2SAL samples, measuring φ1.2 × 3.6 μm and featuring multiple sublayer structures. The observed deformation behavior during compression was the result of the combined action of all sublayers. SEM images and corresponding EDS results confirmed the integrity of the micropillar structures, which were free from defects such as surface cracks, and had clear interfaces between each sublayer. Fig. 6(a–b) displays the microscopic morphologies of the micropillars after uniaxial compression, including detailed views of the deformation. For the TiAlN monolithic micropillar (Fig. 6(a)), cracks initiated from the top layer and propagated downwards, leading to edge cracking. In the TiAlN-2SAL micropillar (shown in Fig. 6(b)), both SALs experienced varying degrees of plastic extrusion. The introduction of SALs allowed the soft layer material to act as a force-sensitive area, yielding first under compression and dissipating compressive stress through plastic deformation. The deformation mode of micropillars altered from brittle fracture, which is typical of pure TiAlN materials, to a coordinated brittle-ductile deformation. The top sublayer experienced compressive stress and underwent brittle cracking, while the ductile layer reduced stress concentration and prevented crack propagation through plastic deformation. As the load increased, the subsequent TiAlN sublayer underwent elastic-plastic deformation, causing the ductile layer to yield sequentially.

Fig. 6(c–d) presents the engineering stress-strain curves of compressing process. The yield strength is defined as the stress at which 0.2 % residual deformation remains after the elastic stage. TiAlN-0SAL micropillars exhibited a predominantly elastic deformation mode, with both elastic limits and yield strengths decreasing as the dual-cycle SALs introduced. The yield strength of the TiAlN-0SAL and TiAlN-2SAL samples were measured at 12.5 GPa and 5.2 GPa, respectively. After yielding, the TiAlN-0SAL samples showed a steady stress increase in a plateau-like manner with further strain, indicating an almost perfectly elastic-plastic behavior [37]. In contrast, the stress-strain data of TiAlN-2SAL samples demonstrated significant strain hardening, which was generally related to the accumulation and interactions of dislocations [38,39]. The deformation of the micropillars was predominantly governed by the plastic flow in the soft layer [40,41]. Thus, the strength of the micropillars was highly contingent on the strength of the soft layers [13], especially given the thickness ratio of the soft layer exceeding 0.05 relative to the micropillar diameter [12]. This also affected the constraint effect of the hard layer on Ti.

To investigate the evolution of microcracks, a specially prepared top-thinned TiAlN-2SAL micropillar was compressed to induce small-scale deformation, as shown in Fig. 6(e). It was observed that the Ti layer had undergone significant plastic deformation, with the TiN layer exhibiting partial cracking. A top view of the micropillar revealed numerous sources where cracks initiated. These cracks originated from surface defects, such as large particles, and progressively propagated downwards through to the SAL, leading to widespread brittle cracking. The reduction in mechanical property of the micropillar was attributed to the thinning of the TiAlN top layer as shown in Fig. S4. The ductile and hard layers gradually yielded from the top, which could serve as a reference for future development of high-strength-tough multilayer coating systems. The fracture strength of micropillars was evaluated by continuous compression until collapse. Fig. 6(f) shows that the TiAlN-0SAL micropillar experienced a significant stress mutation at 6 % deformation, with a distinct 45° shear band observed in its

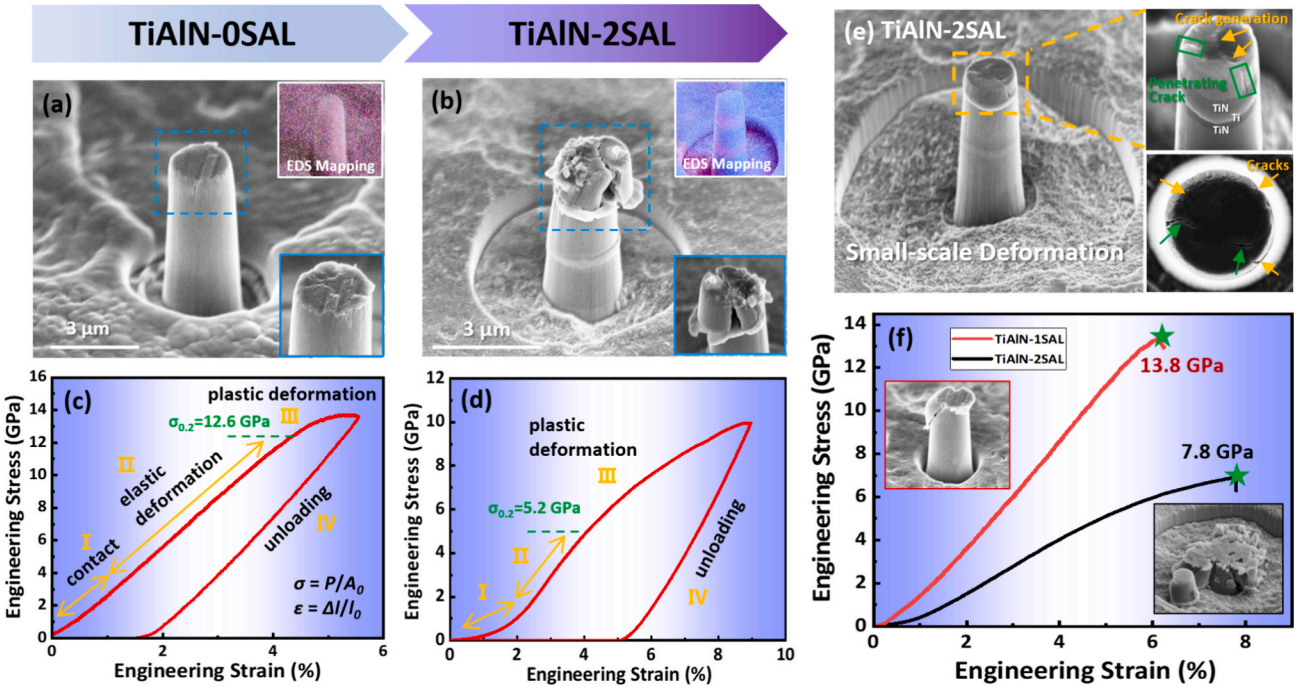

Fig. 6. Micropillar compression results of TiAlN-0SAL and TiAlN-2SAL samples: (a-b) morphological characteristics after compression, (c-d) corresponding stress-strain curves of compression process; (e) crack initiation process in the top-thinned TiAlN-2SAL micropillar with minor load compression, (f) morphological characteristics of TiAlN-0SAL and TiAlN-2SAL micropillars after collapse as well as their stress-strain curves.

micromorphology (see inserted images). The TiAlN monolithic micropillar facilitated an avalanche release of strain through shear fracture, achieving an ultimate compressive strength of 13.8 GPa. In contrast, the TiAlN-2SAL samples exhibited strain bursts, accompanied by obvious brittle cracking. This was due to the fragmentation of all TiAlN sublayers following the plastic extrusion of soft layers. The addition of SALs also altered the fracture behavior of samples. Furthermore, TiAlN-2SAL micropillars exhibited reduced compressive strengths, reaching 7.8

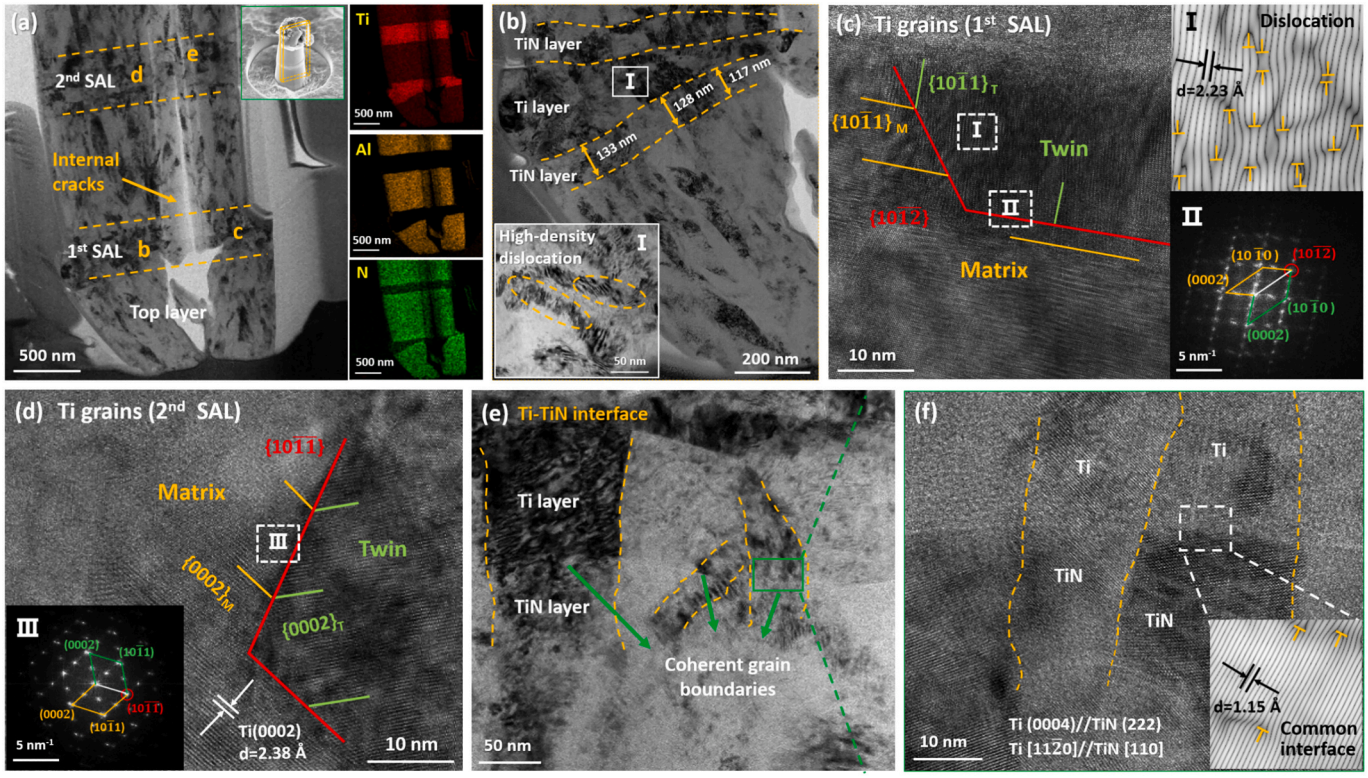

Fig. 7. Structural characterization of TiAlN-2SAL micropillars after compression: (a) TEM internal morphology and EDS results, (b) plastic deformation accompanied by high-density dislocations in the SAL, HRTEM and SAED results of twins in the (c) first and (d) second SAL, (e) HRTEM image of Ti-TiN interface and the (f) partial enlargement information.

GPa. This indicates a failure mode of coordinated brittle-tough deformation triggered by the combined effects of sublayer thinning and compressive strength reduction, thereby enhancing plastic deformation capability.

3.3.2. Microstructural evolution after compression

TEM structural characterization was performed on the TiAlN-2SAL samples after compression to elucidate the strengthening mechanism of the multilayer coating. Fig. 7(a) shows the TEM morphology of a TiAlN-2SAL micropillar cut along the axis. The transparent holes within the micropillar were the result of compression-induced cracks being continuously cut by the FIB. EDS analysis confirmed severe deformation of the top layer and varying degrees of plastic extrusion in the two SALs. The presence of plastic deformation of the first SAL accompanied by high-density dislocations was revealed in the HRTEM near the severely deformed zone (Fig. 7(b)). It can be observed that the Ti and TiN layers exhibited varying degrees of plastic deformation in the vicinity of the crack burst region within the micropillar. It is proposed that the enhanced co-deformability observed in nano-multilayers is due to the high density of interfaces in the metal/ceramic system [42,43]. Furthermore, the heterogeneous interface between the Ti and TiN layers significantly impedes the motion of dislocations, resulting in the accumulation of dislocations within the Ti layer [44]. This absorption of strain energy increases the stress required for further plastic deformation.

Fig. 7(c–d) shows the $\{10\bar{1}2\}$ and $\{10\bar{1}1\}$ twin boundaries (TBs) in different SALs, respectively. The images showed twin boundaries, indicated by red lines, and the traces of matrix and basal planes in the twins, marked by yellow and green dashed lines. In region I, a significant number of dislocations accumulated at the twin edges, and the twin boundaries prevented further dislocation movement. In region II, the grains on either side of the twin boundary had parallel basal and prismatic planes, known as BP/PB steps [45,46]. The twin boundaries themselves consisted of long 90° BP/PB steps and $(10\bar{1}2)$ twin planes, which resulted in the twin orientations deviating from theoretical predictions [47]. In regions II and III, the basal planes of the matrix and twin crystals displayed multiple orientations that were not perpendicular to the twin boundaries. Small-scale selected area electron diffraction (SAED) images were taken II–III, including the twin boundaries. The images demonstrated that the typical matrix and twins share diffraction spots, indicating a coherent structural relationship. This phenomenon suggests that the generation of deformation twins, along with the high-density distribution of dislocations on these twin boundaries, plays a crucial role in reducing the strain energy caused by deformation. Furthermore, it enhances the plasticity and ductility of the material by inhibiting dislocation slip [48,49].

Fig. 7(e) displays the HRTEM image of the Ti-TiN interface within the deformation zone of the second SAL, while Fig. 7(f) provides a detailed enlargement. The images revealed numerous coherent interfaces at the Ti-TiN biphasic grain boundaries, with the grain continuing along these boundaries. The formation of the metal/ceramic coherent interfaces is a result of the gradient transition design implemented during deposition. The design effectively reduces the elastic strain energy at the interfaces and restricts the plastic flow of the metal layer [50].

3.4. Elastoplastic deformation mechanism

To elucidate the deformation mechanism of TiAlN-based multilayer coatings under compression, Fig. 8 offers a schematic representation of the damage behavior from a structural evolution perspective. The deformation process of TiAlN monolithic micropillars, as shown in Fig. 8 (a), started with radial cracks originating from surface defects on the micropillars and progressively spreading as the strain increases. The TiAlN hard layer, exhibited greater brittleness and reduced fracture toughness, resulting in strain bursts through a 45° slip band accompanied by brittle cracking throughout micropillar. Fig. 8(b) shows the enhanced cracking resistance of the coatings after the introduction of a dual-cycle SALs. Compression induced a deformation process dominated by the plastic flow of the Ti layer. Cracks were deflected or halted upon reaching the SAL due to the unique soft/hard alternating stress-absorbed structure of TiN-Ti-TiN. Plastic deformation of the SALs initiated near the top layer, followed by the expansion and radial penetration of microcracks on the top layer. Severe brittle fracture was observed when the TiAlN top layer was compressed beyond its ultimate strength, with interfacial slip occurring in the direction of the Ti layer's plastic flow. Furthermore, new microcracks were formed at the slip interface and propagated downwards. The fracture process was further mitigated by the second SALs through severe plastic extrusion. In this case, the ductile layers yielded sequentially to alleviate stress concentration, significantly

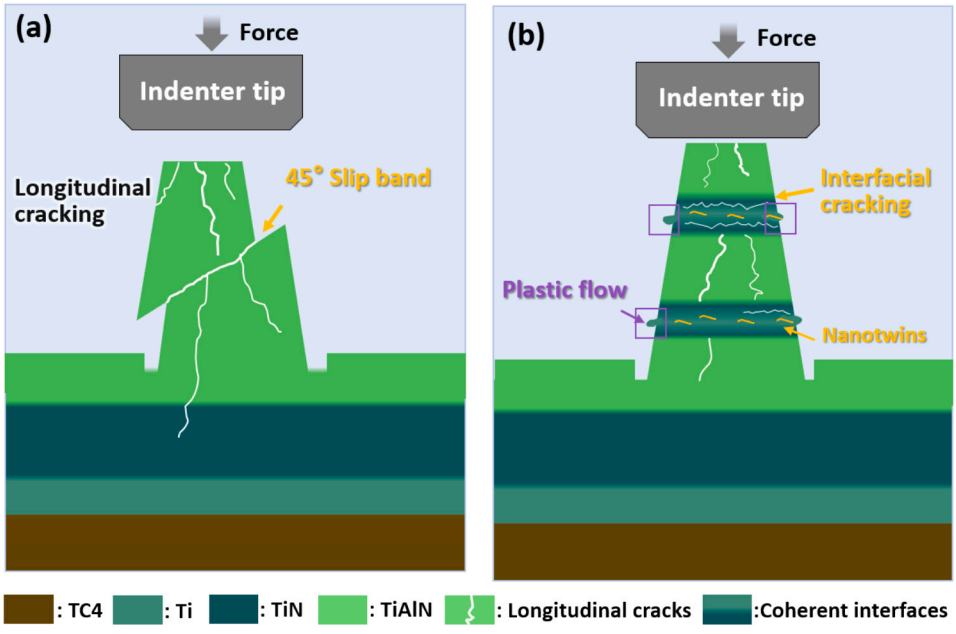

Fig. 8. Schematic diagram of the compression failure mechanism for Ti/TiN/TiAlN based multilayer coatings: (a) TiAlN-0SAL samples, (b) TiAlN-2SAL samples.

enhancing the plastic deformation capability and inhibiting failure.

4. Conclusions

TiAlN-based multilayer coatings with varying numbers of stress-absorbed layers (SALs) were prepared on titanium alloy by cathode vacuum arc ion plating. The correlation between the mechanical behavior of the coatings and their periodic structure was investigated, and the strengthening mechanism was characterized. The detailed results were summarized as follows:

(1) The study revealed that the TiAlN-2SAL samples, which exhibit a dual-cycle soft/hard alternating structural arrangement, demonstrated the highest bonding force (67.9 N) and crack resistance. Furthermore, they exhibited enhanced fracture toughness (11.29 $MPa{\cdot}m^{1/2}$) and superior erosion resistance (0.04 ± 0.008 mg/g).
(2) The results of the uniaxial compression tests indicated that the hard layer had a limited impact on the plastic deformation of the soft layer. The primary deformation behavior was attributed to the plastic flow of titanium. The strength of the micropillars was found to be primarily determined by the yield stress of the Ti layers, which was found to be significantly affected by cyclic modulation.
(3) The incorporation of SALs augmented the number of interfaces within the materials, thereby facilitating the accumulation of slip dislocations and enhancing the interface energy. Consequently, the stress required for further plastic deformation was elevated. SALs improved the material's resistance to crack propagation by forming nanotwins and coherent interfaces, which decelerated the delamination process.
(4) Co-deformation prior to cracking was observed in SALs. This enhanced co-deformability in metal/ceramic nano-multilayers indicated that the TiN layer remains plastically deformed under compression until dislocations in the Ti layer cross over the interface to the TiN layer without causing cracks. As the stress continued to increase, the deformation mechanism underwent a shift towards a coordinated brittle-tough deformation process. This phenomenon is characterized by the initiation and expansion of microcracks in the top layer of TiAlN, accompanied by brittle damage in the hard layer and durably plastic flow in the ductile layer.

CRediT authorship contribution statement

Jingjun Yan: Writing – original draft, Investigation, Formal analysis. **Zhenyu Wang:** Supervision, Funding acquisition. **Shenghao Zhou:** Writing – review & editing, Funding acquisition. **Guanshui Ma:** Formal analysis, Conceptualization. **Dingwei Zhou:** Investigation, Data curation. **Wei Yang:** Formal analysis, Conceptualization. **Aiying Wang:** Writing – review & editing, Investigation, Funding acquisition.

Declaration of competing interest

The authors declare that they have no known competing financial interests or personal relationships that have appeared to influence the work reported in this paper.

Data availability

Data will be made available on request.

Acknowledgements

The authors would like to acknowledge the National Science Found for Distinguished Young Scholars of China (No. 52025014), the National Natural Science Foundation of China (No. 52171090), the Natural Science Foundation of Zhejiang Province (No. LQ23E010002), and the Natural Science Foundation of Ningbo Municipality (No. 2023J410). We also would like to give thanks to Danli Zhang from Xi'an Jiaotong University for micropillar compression tests.

Appendix A. Supplementary data

Supplementary data to this article can be found online at https://doi.org/10.1016/j.surfcoat.2024.131187.

References

[1] V. Bonu, S. Kumar, P.N. Sooraj, H.C. Barshilia, A novel solid particle erosion resistant Ti/TiN multilayer coating with additional energy absorbing nano-porous metal layers: validation by FEM analysis, Mater. Des. 198 (2021) 109389.
[2] K. Shukla, R. Rane, J. Alphonsa, P. Maity, S. Mukherjee, Structural, mechanical and corrosion resistance properties of Ti/TiN bilayers deposited by magnetron sputtering on AISI 316L, Surf. Coat. Technol. 324 (2017) 167–174.
[3] F. Liang, Y. Shen, C. Pei, B. Qiu, J. Lei, D. Sun, Microstructure evolution and corrosion resistance of multi interfaces Al-TiAlN nanocomposite films on AZ91D magnesium alloy, Surf. Coat. Technol. 357 (2019) 83–92.
[4] V. Bonu, M. Jeevitha, V.P. Kumar, S. Bysakh, H.C. Barshilia, Ultra-thin multilayered erosion resistant Ti/TiN coatings with stress absorbing layers, Appl. Surf. Sci. 478 (2019) 872–881.
[5] J. Shuai, X. Zuo, Z. Wang, P. Guo, B. Xu, J. Zhou, A. Wang, P. Ke, Comparative study on crack resistance of TiAlN monolithic and Ti/TiAlN multilayer coatings, Ceram. Int. 46 (5) (2020) 6672–6681.
[6] X. Cai, Y. Gao, F. Cai, L. Zhang, S. Zhang, Effects of multi-layer structure on microstructure, wear and erosion performance of the Cr/CrN films on Ti alloy substrate, Appl. Surf. Sci. 483 (2019) 661–669.
[7] H. Zhang, Z. Li, W. He, C. Ma, J. Chen, B. Liao, Y. Li, Damage mechanisms evolution of TiN/Ti multilayer films with different modulation periods in cyclic impact conditions, Appl. Surf. Sci. 540 (2021) 148366.
[8] N. Li, X.Y. Liu, Mechanical behavior of metal/ceramic interfaces in nanolayered composites—experiments and modeling, J. Mater. Sci. 53 (2018) 5562–5583.
[9] G. Dehm, B.N. Jaya, R. Raghavan, C. Kirchlechner, Overview on micro-and nanomechanical testing: new insights in interface plasticity and fracture at small length scales, Acta Mater. 142 (2018) 248–282.
[10] X. Zhang, B. Zhang, Y. Mu, S. Shao, C.D. Wick, B.R. Ramachandran, W.J. Meng, Mechanical failure of metal/ceramic interfacial regions under shear loading, Acta Mater. 138 (2017) 224–236.
[11] S. Lotfian, M. Rodríguez, K.E. Yazzie, N. Chawla, J. Llorca, J.M. Molina-Aldareguía, High temperature micropillar compression of Al/SiC nanolaminates, Acta Mater. 61 (12) (2013) 4439–4451.
[12] L.W. Yang, C. Mayer, N. Li, J.K. Baldwin, N.A. Mara, N. Chawla, J.M. Molina-Aldareguia, J. Llorca, Mechanical properties of metal-ceramic nanolaminates: effect of constraint and temperature, Acta Mater. 142 (2018) 37–48.
[13] D.Q. Doan, T.H. Fang, T.H. Chen, Interfacial and mechanical characteristics of TiN/Al composites under nanoindentation, Int. J. Solids Struct. 226 (2021) 111083.
[14] W. Yang, G. Ayoub, I. Salehinia, B. Mansoor, H. Zbib, Deformation mechanisms in Ti/TiN multilayer under compressive loading, Acta Mater. 122 (2017) 99–108.
[15] J.M. Wheeler, C. Harvey, N. Li, A. Misra, N.A. Mara, X. Maeder, J. Michler, S. Pathak, High temperature nanoindentation of Cu-TiN nanolaminates, Mater. Sci. Eng. A 804 (2021) 140522.
[16] L. Zhang, Y.Q. Shen, Y.M. Zhao, S.N. Chen, X. Ouyang, X. Zhang, H. Liang, B. Liao, L. Chen, Structure control of high-quality TiAlN monolithic and TiAlN/TiAl multilayer coatings based on filtered cathodic vacuum arc technique, Surf. Interfaces 38 (2023) 102836.
[17] J. Kübarsepp, K. Juhani, M. Tarraste, Abrasion and erosion resistance of cermets: a review, Materials 15 (1) (2021) 69.
[18] H. Ruan, Z. Wang, L. Wang, L. Sun, H. Peng, P. Ke, A. Wang, Designed Ti/TiN sub-layers suppressing the crack and erosion of TiAlN coatings, Surf. Coat. Technol. 438 (2022) 128419.
[19] D. Zhou, Z. Wang, Y. Zhang, J. Yan, G. Ma, X. Hu, P. Ke, A. Wang, Stimulated corrosion damage of Ti-Al-N multilayer coatings under interval salt spray and hot condition, Corros. Sci. 222 (2023) 111431.
[20] J. Shuai, X. Zuo, Z. Wang, L. Sun, R. Chen, L. Wang, A. Wang, P. Ke, Erosion behavior and failure mechanism of Ti/TiAlN multilayer coatings eroded by silica sand and glass beads, J. Mater. Sci. Technol. 80 (2021) 179–190.
[21] R.L. Boxman, S. Goldsmith, Principles and applications of vacuum arc coatings, IEEE Trans. Plasma Sci. 17 (5) (1989) 705–712.
[22] A.N. Panckow, J. Steffenhagen, B. Wegener, L. Dübner, F. Lierath, Application of a novel vacuum-arc ion-plating technology for the design of advanced wear resistant coatings, Surf. Coat. Technol. 138 (1) (2001) 71–76.
[23] S. Zhang, X. Zhang, Toughness evaluation of hard coatings and thin films, Thin Solid Films 520 (7) (2012) 2375–2389.
[24] V. Bonu, M. Jeevitha, V. Praveen Kumar, G. Srinivas, Siju, H.C. Barshilia, Solid particle erosion and corrosion resistance performance of nanolayered multilayered Ti/TiN and TiAl/TiAlN coatings deposited on Ti6Al4V substrates, Surf. Coat. Technol. 387 (2020) 125531.
[25] K. Chu, K. Yan, F. Ren, Q. Sun, A dual-pillar method for measurement of stress-strain response of material at microscale, Scr. Mater. 172 (2019) 138–143.

[26] S. Shim, H. Bei, M.K. Miller, G.M. Pharr, E.P. George, Effects of focused ion beam milling on the compressive behavior of directionally solidified micropillars and the nanoindentation response of an electropolished surface, Acta Mater. 57 (2) (2009) 503–510.
[27] F. Xiao, K. Chu, Z. Li, R. Hou, Y. Gao, Q. Sun, X. Jin, Improved functional fatigue resistance of single crystalline NiTi micropillars with uniformly oriented Ti_3Ni_4 precipitates, Int. J. Plast. 160 (2023) 103480.
[28] M. Simsir, Y. Palaci, A. Özer, A comparative study of hardness/scratch/wear properties of TiCN and TiAlN coatings on DIN 1.2842 steel by CA-PVD method, J. Aust. Ceram. Soc. 57 (4) (2021) 1027–1037.
[29] A.R. Shugurov, M.S. Kazachenok, Mechanical properties and tribological behavior of magnetron sputtered TiAlN/TiAl multilayer coatings, Surf. Coat. Technol. 353 (2018) 254–262.
[30] Y. Xie, H.M. Hawthorne, Effect of contact geometry on the failure modes of thin coatings in the scratch adhesion test, Surf. Coat. Technol. 155 (2–3) (2002) 121–129.
[31] J.Y. Zhang, X. Zhang, R.H. Wang, S.Y. Lei, P. Zhang, J.J. Niu, G. Liu, G.J. Zhang, J. Sun, Length-scale-dependent deformation and fracture behavior of Cu/X (X = Nb, Zr) multilayers: the constraining effects of the ductile phase on the brittle phase, Acta Mater. 59 (19) (2011) 7368–7379.
[32] S. Bigelow, Y.L. Shen, Indentation-induced shear band formation in thin-film multilayers, Front. Mater. 4 (2017) 25.
[33] S. Zhang, D. Sun, Y. Fu, H. Du, Toughness measurement of thin films: a critical review, Surf. Coat. Technol. 198 (1–3) (2005) 74–84.
[34] R. Ali, M. Sebastiani, E. Bemporad, Influence of Ti–TiN multilayer PVD-coatings design on residual stresses and adhesion, Mater. Des. 75 (2015) 47–56.
[35] R. Saha, W.D. Nix, Effects of the substrate on the determination of thin film mechanical properties by nanoindentation, Acta Mater. 50 (1) (2002) 23–38.
[36] H. Zhang, Z. Li, W. He, B. Liao, G. He, X. Cao, Y. Li, Damage evolution and mechanism of TiN/Ti multilayer coatings in sand erosion condition, Surf. Coat. Technol. 353 (2018) 210–220.
[37] S.H. Li, Y. Zhao, J. Radhakrishnan, U. Ramamurty, A micropillar compression investigation into the plastic flow properties of additively manufactured alloys, Acta Mater. 240 (2022) 118290.
[38] S.H. Li, Y. Zhao, P. Kumar, U. Ramamurty, Effect of initial dislocation density on the plastic deformation response of 316L stainless steel manufactured by directed energy deposition, Mater. Sci. Eng. A 851 (2022) 143591.
[39] A.S. Schneider, D. Kiener, C.M. Yakacki, H.J. Maier, P.A. Gruber, N. Tamura, M. Kunz, A.M. Minor, C.P. Frick, Influence of bulk pre-straining on the size effect in nickel compression pillars, Mater. Sci. Eng. A 559 (2013) 147–158.
[40] M. Nasim, Y. Li, M. Wen, C. Wen, A review of high-strength nanolaminates and evaluation of their properties, J. Mater. Sci. Technol. 50 (2020) 215–244.
[41] R. Raghavan, J.M. Wheeler, D. Esqué-De los Ojos, K. Thomas, E. Almandoz, G. G. Fuentes, J. Michler, Mechanical behavior of Cu/TiN multilayers at ambient and elevated temperatures: stress-assisted diffusion of Cu, Mater. Sci. Eng. A 620 (2015) 375–382.
[42] N. Li, H. Wang, A. Misra, J. Wang, In situ nanoindentation study of plastic co-deformation in Al-TiN nanocomposites, Sci. Rep. 4 (1) (2014) 6633.
[43] D. Bhattacharyya, N.A. Mara, P. Dickerson, R.G. Hoagland, A. Misra, A transmission electron microscopy study of the deformation behavior underneath nanoindents in nanoscale Al–TiN multilayered composites, Philos. Mag. 90 (13) (2010) 1711–1724.
[44] S.H. Li, Y. Zhao, U. Ramamurty, Role of the solidification cells on the yield strength of the Al-Si-Mg alloy manufactured using laser powder bed fusion: a micropillar compression study, Scr. Mater. 234 (2023) 115566.
[45] H.C. Wu, Y.X. Yu, X.F. Bi, Atomic scale structural characterization of $\{10\bar{1}2\}$ twin boundaries in zinc, Trans. Nonferrous Met. Soc. China 28 (8) (2018) 1538–1542.
[46] J. Wang, L. Liu, C.N. Tomé, S.X. Mao, S.K. Gong, Twinning and de-twinning via glide and climb of twinning dislocations along serrated coherent twin boundaries in hexagonal-close-packed metals, Mater. Res. Lett. 1 (2) (2013) 81–88.
[47] B. Xu, L. Capolungo, D. Rodney, On the importance of prismatic/basal interfaces in the growth of twins in hexagonal close packed crystals, Scr. Mater. 68 (11) (2013) 901–904.
[48] S. Zhao, R. Zhang, Q. Yu, J. Ell, R.O. Ritchie, A.M. Minor, Cryoforged nanotwinned titanium with ultrahigh strength and ductility, Science 373 (6561) (2021) 1363–1368.
[49] J. Yuan, S. Zhou, H. Wu, Z. Wang, Y. Zhang, G. Zhou, G. Ma, P. Ke, A. Wang, Ultrahigh strength-ductility of nanocrystalline Cr2AlC coating under micropillar compression, Scr. Mater. 235 (2023) 115594.
[50] K. Lu, L. Lu, S. Suresh, Strengthening materials by engineering coherent internal boundaries at the nanoscale, Science 324 (5925) (2009) 349–352.